

Observations of ice thickness and frazil ice in the St. Lawrence Island polynya from satellite imagery, upward looking sonar, and salinity/temperature moorings

Robert Drucker and Seelye Martin

School of Oceanography, University of Washington, Seattle, Washington, USA

Richard Moritz

Polar Science Center/Applied Physics Laboratory, University of Washington, Seattle, Washington, USA

Received 13 November 2001; revised 20 November 2002; accepted 27 February 2003; published 17 May 2003.

[1] For the 1999 winter, this paper examines the behavior of the Bering Sea St. Lawrence Island polynya using a combination of Advanced Very High Resolution Radiometer (AVHRR), RADARSAT synthetic aperture radar (SAR), meteorological data, over-winter moored upward looking sonars (ULS) and SeaBird salinity/temperature sensors. We define a thermal ice thickness from the AVHRR retrieval of ice surface temperature combined with meteorological observations and a heat flux model. South of the island, we compare the ULS and thermal thicknesses for congelation and frazil ice. When the satellites observe congelation ice over the ULSS, the ULS and thermal ice thicknesses generally agree. When SAR observes Langmuir plumes over the ULSS, which indicate frazil ice formation, the ULSS show scatterers at 5–20 m depths in the water column and the seawater temperatures are either within 0.01°C of freezing or are slightly supercooled. This suggests that during frazil events, crystals either nucleate at depth or are transported to depth by the Langmuir circulation. The combination of the SAR imagery and ULS observations also allow measurement of the pack ice advection velocity, the polynya width and the downwind frazil accumulation thickness, giving widths of 10 to 30 km and thicknesses of 0.1–0.2 m. Substitution of these observed values with the heat flux into the Pease polynya model yields polynya widths that approximately agree with the observed.

INDEX TERMS: 4207 Oceanography: General: Arctic and Antarctic oceanography; 4243 Oceanography: General: Marginal and semienclosed seas; 4275 Oceanography: General: Remote sensing and electromagnetic processes (0689); 4540 Oceanography: Physical: Ice mechanics and air/sea/ice exchange processes; *KEYWORDS:* St. Lawrence Island polynya, Bering Sea, polynya processes, remote sensing studies of polynyas

Citation: Drucker, R., S. Martin, and R. Moritz, Observations of ice thickness and frazil ice in the St. Lawrence Island polynya from satellite imagery, upward looking sonar, and salinity/temperature moorings, *J. Geophys. Res.*, 108(C5), 3149, doi:10.1029/2001JC001213, 2003.

1. Introduction

[2] Because of the accompanying large heat and salt fluxes, the presence and growth of frazil and thin ice in polynyas play a critical role in the linkage of the atmospheric heat budget with the ice mass balance and the oceanic salt budget. To this date, however, there has been no validation of the analytic and numerical polynya models with measurements in large polynyas. As part of a 1999 winter polynya field experiment, two moored upward-looking sonars (ULSS) as well as current meter and SeaBird salinity/temperature moorings were deployed south of St. Lawrence Island in the Bering Sea. Figure 1 shows the location of the ULS and SeaBird sensors used in this study. The purpose of this

over-winter deployment was to study the ice and ocean response to the polynya events that occur south of the island during periods of cold northerly winds. For the same period, the visible-infrared Advanced Very High Resolution Radiometer (AVHRR) and Synthetic Aperture Radar (SAR) imagery of the region provide information on the areal distribution of ice properties. The combination of the field and satellite observations allows determination of the properties of frazil ice formation, permits comparison of the ULS observations of ice thickness with those made by remote sensing, and also permits comparison of the observed frazil thickness and polynya widths with model results.

[3] Coastal polynyas form when offshore winds advect the pack away from the coast, so that the resultant open water is exposed to cold air temperatures and strong winds. The winds generate waves on the open water surface, where the wave amplitudes and wavelengths increase with dis-

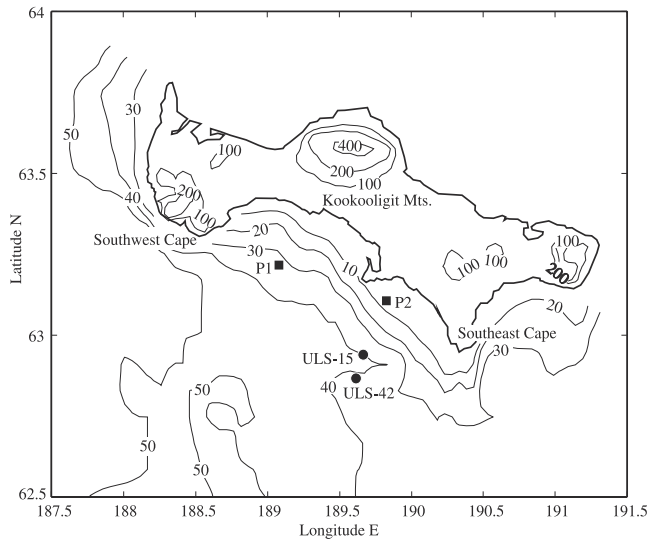


Figure 1. Chart of the St. Lawrence Island region, showing the ULS and SeaBird locations. Solid squares show the SeaBird moorings P1 and P2; solid circles show the combined ULS and SeaBird moorings. For scale, the separation between P1 and P2 is 40.5 km; between ULS-15 and ULS-42 it is 8.8 km. Contour lines are labeled in meters; the inshore depths are approximate (bottom data courtesy of Scientific Fishery Systems, Anchorage, Alaska).

tance from the coast. As the polynya width increases, the interaction of the waves with the wind stress creates a Langmuir circulation in the water column, which consists of vortices with the rotor axes approximately parallel to the surface winds and where adjacent rotors turn in opposite directions [Martin, 1981]. In the absence of a halocline, the rotor diameter approximately equals the bottom depth. Tank experiments and river observations cited by Martin [1981] suggest that the mixing induced by this circulation either cools the entire column to the freezing temperature or slightly supercools it. This means that ice formation occurs initially throughout the water column in the form of small millimeter-scale crystals, called frazil crystals, which float slowly to the surface.

[4] Once these crystals reach the surface, the circulation herds them into long bands or plumes of grease ice located at the Langmuir convergence zones, where the plumes are approximately parallel to the surface wind and are visible on SAR imagery [Liu et al., 1997]. These highly viscous frazil plumes with thicknesses of order 10 cm damp out the short incident waves. As the plumes grow downwind, they become wider and increase in thickness. As their thickness increases, they begin to freeze at the surface. The longer waves propagating through this newly formed ice break it into floes with diameters of 0.3 to 0.5 m, called pancake ice. The frazil and pancake ice are then advected downwind by the wind stress, where this ice accumulates against the edge of the solid pack ice, and eventually freezes solid.

[5] Previous field and theoretical studies of the St. Lawrence Island polynya region include the over-winter moorings of Schumacher et al. [1983], the aircraft observations and modeling effort of Pease [1987] and the recent numerical polynya model of Morales Maqueda and Will-

mott [2000]. In related work, Winsor and Björk [2000] model the polynya ice production around the entire Arctic Basin, and Haarpaintner et al. [2001] compare model and satellite observations of the Storfjorden polynya. Each of the above numerical polynya models is based on work by Pease [1987], who calculates the downwind length of the active Langmuir plume region based on the steady state assumption that there is a balance between the downwind export of the pack ice surrounding the polynya, against which the frazil/pancake ice accumulates, and the upwind growth of the accumulated frazil. In all these models, the unknown parameter is the solid ice equivalent of the frazil accumulation thickness at the downwind polynya edge. The reason for use of the solid ice equivalent is that frazil ice is a slurry of water and ice, while the accumulation thickness represents the total ice growth and is thus less thick than the frazil ice. For descriptive purposes, we refer to the frazil ice in the Langmuir region as active frazil, the ice immediately downwind of the active frazil as accumulated frazil, where this ice is at least in part an ice/water slurry, and the frozen mixture of columnar and frazil ice surrounding the polynya as consolidated ice.

[6] The Pease [1987] steady state model describes the polynya size in terms of four variables: the export velocity U_I of the pack ice away from the polynya region, the heat loss F_F from the frazil region given in terms of ice growth with units of m s^{-1} , the polynya width R , and the solid ice equivalent h_C of the frazil accumulation thickness. With these definitions, Pease [1987] shows that

$$R = h_C U_I / F_F. \quad (1)$$

For some examples of accumulation thicknesses, Pease [1987] assumes that h_C is between 5 and 30 cm, Haarpaintner et al. [2001] assume $h_C = 20$ cm, and Winsor and Björk [2000] assume that the accumulation thickness is a linear function of 10-m wind speed that increases from 10 to 30 cm as the wind speed increases from 5 to 35 m s^{-1} . In their numerical model, Morales Maqueda and Willmott [2000] choose $h_C = 10$ cm, and Biggs et al. [2000] set $h_C = 48$ cm. In the above papers, h_C is generally chosen such that the calculated polynya widths match the satellite observations. Because h_C is not a true thickness, but rather the solid ice equivalent thickness of the mass of frazil ice per unit area, it is difficult to measure. The only field observation of the accumulation thickness is from a small 50 m long lead, where for an air temperature of -16°C and a 10 m s^{-1} wind speed, Martin and Kaufman [1981] observe that the accumulated frazil ice thickness is 5–8 cm. On the basis of their laboratory observations showing that the accumulated frazil has an ice volume fraction of about 40%, $h_C = 2$ –3 cm.

[7] For measurements of h_C , the following discussion shows that when the accumulated frazil freezes solid, our AVHRR technique permits direct measurement of the ice thickness over a large area. Because we cannot tell from this observation whether the frazil ice is completely frozen in the vertical, this AVHRR inferred measurement may underestimate h_C . In contrast, the ULS observations permit point measurements of the accumulation depths that are independent of whether the frazil ice layer is completely frozen. The combination of these techniques allows determination

of the accumulation depth in a number of cases. Because our data also allows us to measure the pack ice export velocity from successive SAR images, the polynya width from single SAR images, and the ice growth rate from the meteorological measurements, all of the variables in equation (1) can be directly measured, which permits comparison of the observed and predicted polynya widths. The results show that our ULS accumulation thicknesses are comparable to the theoretical models and that the observed and calculated polynya widths approximately agree.

[8] The paper proceeds as follows: Section 2 describes the ULSs and their observational errors; section 3 describes the SAR polynya observations and compares the ULS observations of deep scatterers with the meteorological forcing and the SAR-observed polynya events. Section 4 describes the AVHRR ice thickness algorithm and its uncertainties, then applies the algorithm to AVHRR images of frazil and congelation ice polynyas. Section 5 presents a detailed comparison of the AVHRR and ULS ice thicknesses; section 6 compares our observations to the *Pease* [1987] polynya model and shows that the derived polynya widths approximately agree with the observed; section 7 compares the ULS observations of deep scatterers with the SeaBird observations of near-freezing and supercooled water at depth. Section 8 gives our conclusions.

2. ULS Estimates of Ice Thickness

[9] The ULS functions by focusing acoustic energy into a narrow pulsed beam, then measuring the elapsed time for the pulse to propagate to the target and back. The pulse frequency and length are respectively 300 kHz and 1 ms. The detection threshold is set low enough that echoes from the interfaces between seawater and air, and between seawater and congelation ice, are detected at ranges of 30–100 m. The threshold is also set high enough that at these ranges, echoes from phytoplankton blooms or from a 1°C thermocline step are not detected.

[10] Similar moored instruments have been used many times to provide estimates of sea ice draft [e.g., *Hudson*, 1990; *Pilkington and Wright*, 1991; *Melling et al.*, 1995; *Strass*, 1998; *Vinje et al.*, 1998]. The ULS is a 0.43-m diameter spherical glass float that contains a microprocessor, power supply, precision pressure gauge and thermistor. Ambient water pressure is measured through a port. The thermistor is mounted inside the pressure gauge, and its readings are used to correct for temperature dependence of the pressure calibration coefficients. The pulse is emitted by a ceramic transducer mounted on a gimbal inside an acoustic lens located outside and at the top of the sphere. The gimbal is weighted so the pulse propagates vertically. The lens focuses the pulse to a narrow beam with a nominal half-power beam width of 2°, so that for a ULS depth of 34 m, the beam footprint on the water surface has a 1.2-m diameter. The two ULSs used in the experiment are labeled ULS-15 and ULS-42. After recovery, the ULS-42 acoustic lens was found to contain a small water bubble. As we show below, the effect of this bubble was to reduce the sensitivity of ULS-42 relative to ULS-15, and to give its measurements slightly larger error bars. Figure 1 and Table 1 give the locations, depths and deployment periods for the two ULSs and for the SeaBird conductivity/temperature sensors used

Table 1. Location, Depths and Deployment Periods for the Two ULSs and for the SeaBird Salinity/Temperature Sensors

	ULS-15	UL-42	P1	P2
Position	62.93°N, 170.33°W	62.87°N, 170.38°W	63.22°N, 170.92°E	63.11°N, 170.17°E
Relative Location	Nearshore	Offshore		
Water depth	44 m	45 m	33 m	33 m
ULS depth	33–34 m	33.5–34.5 m		
SeaBird depth	39 m	40 m	30 m	29 m
Deployed	12 Sept 1998	13 Sept 1998	9 Sept 1998	21 Sept 1998
Recovered	17 Sept 1999	17 Sept 1999	14 Sept 1999	13 Sept 1999

in this analysis; Appendix A describes the detailed ULS operation. Because the bathymetry is not accurate close to the island, the depth of P2 observed during deployment and listed in the table does not agree with Figure 1.

[11] To make efficient use of battery power, the ULS takes low-resolution samples at 5-min intervals throughout the deployment. In addition, twice per day from 0000 to 0025 GMT and 1200 to 1225 GMT, the ULS takes high-resolution samples at 10-s intervals to resolve individual features such as ridges, smooth ice, and leads as they drift over the mooring. The ULS also measures two different kinds of returns. The first return is the first received signal that exceeds the detection threshold, and gives the depth of the deepest detectable targets in the footprint. The target could be the deepest consolidated ice, or material suspended in the water column such as air bubbles, frazil, sediment, fish and concentrations of zooplankton. The last valid return is the last distinct, detectable signal received, and provides an indication of the shallowest detectable targets in the footprint. As Appendix A describes, the ULS estimates the ice draft h for both returns; these are converted to ice thickness h_{ULS} through the relation

$$H_{ULS} = 1.1h. \quad (2)$$

Equation (2) yields the first and last valid return ice thicknesses; these variables are regarded as simple estimates of the thickest and thinnest detectable ice in the sonar footprint.

2.1. ULS Errors

[12] ULS errors divide into random and systematic errors. As Appendix A describes, the two dominant errors in determination of the ice draft are the 3 mbar uncertainty in the NCEP sea level pressure, which translates to a thickness error of ± 3 cm; and the round-off error in the pressure gauge, which amounts to ± 2 cm. Because the round-off error tends to zero when averaged, the uncertainty of the average offset is taken to be ± 3 cm. The instruments also have a systematic offset error of less than 5 cm relative to the free surface. The origin of this offset is unknown, but potential culprits include systematic deviations of the sonar electronic components from their specifications, and systematic differences between the mean temperature and salinity of the water column and the values measured just below the ULS.

[13] This offset is estimated by inspecting the high-resolution time series for intervals of nearly level targets, then identifying the interval with the minimum apparent ice draft

as open water. Because this minimum draft should be zero, we adjust the entire time series for the given ULS by the constant offset that sets the ice draft to zero for the selected interval. The selected intervals and associated offsets are as follows: for ULS-15, 29 April 1999 at 1200 UT and -1 cm; for ULS-42, 10 April 1999 at 1200 GMT and -3 cm, with a relative accuracy of about ± 1 cm. As a check on this procedure, we searched the low-resolution ice draft time series for the entire winter for clusters of adjusted ice drafts that remain below zero, and might indicate another occurrence of open water. In this search, we found only a few clusters with adjusted ice drafts in the range $0 \leq h < 3$ cm.

[14] Finally, because the offset is subtracted from every observation, each of which has the uncertainties given above, this means that the total RMS uncertainty of the observations is about ± 5 cm. This is true only for thin flat ice and open water, as *Melling et al.* [1995] describe, there are additional uncertainties associated with thickness measurements in rough ice that amount to no more than a few percent of ice thickness.

2.2. Scattering in the Water Column

[15] The preceding error analysis applies to pulses reflected from a nearly level ice/water or water/air interface in the sonar footprint. Confidence in this analysis is bolstered by the fact that the two instruments give very similar results for the last valid return ice draft. In certain portions of the yearlong record however, we find large discrepancies between the depths of the first returns. In this discussion, the term Day refers to the day-of-year, so that for 1999, December 31, 1998, is Day 0, such that Day 1 is coincident with January 1, 1999, and so forth. In particular, during autumn 1998 (Days 250–300 in 1998) and summer 1999 (Days 180–250) there are several 1–3 day periods in which the ULS first return suggests the presence of scatterers deep in the water column. During these periods, ice and meteorological charts show that the ocean south of St. Lawrence Island was ice-free and the winds were strong. This suggests that the scatterers are probably air bubbles entrained in the water column by breaking waves or sediment entrained from the ocean bottom.

[16] For the autumn 1998 and summer 1999 stormy periods, the first return depths at ULS-15 are consistently approximately twice those at ULS-42. Given that both instruments are in water of about the same depth, and as Figure 1 shows, the horizontal distance between the two instruments is only 9 km, or much smaller than both the distance from ULS-15 to the coast and the typical space scale of wind variability associated with storms, we expect that the distribution of scatterers in the water column should be approximately the same at the two locations. If so, this difference in response implies a difference in sensitivity between the two ULS. This sensitivity difference is qualitatively consistent with the observation made at recovery that the acoustic lens on ULS-42 contained a small water bubble that causes slight defocusing, while the lens on ULS-15 was bubble-free.

[17] The different sensitivities of ULS-42 and ULS-15 limit the extent to which we can interpret differences in deep scattering observations by the two instruments during the winter frazil ice events. As we show below, in some cases ULS-15 observes scatterers at depths 10–15 times greater

than the depths reported by ULS-42. Without independent information on how target strength varies with depth in (1) wave-generated bubble layers and (2) frazil ice, we cannot say whether the scatterers are really deeper at ULS-15 than at ULS-42, or whether the differences in instrument sensitivity account for these observations.

[18] One of the problems in this paper is our inability to distinguish at depth between air bubbles and frazil ice. Air bubbles in the water column are produced by breaking waves whereas frazil ice is produced by heat loss from a turbulent water surface at a freezing temperature. Layers of air bubbles generated by wave breaking cause substantial reverberation of high-frequency sonar. For example, target strengths observed by *Crawford and Farmer* [1987] at 119 kHz under wind speeds ranging from $7\text{--}11$ m s⁻¹ would produce a larger ULS signal than flat or sloping congelation ice and would therefore be detected. For conditions of high wind and open seas, *Farmer and Li* [1995] show that the Langmuir circulation can organize the suspended bubbles into patterns extending 10 or more meters below the sea surface. Due to buoyancy effects, the number, density, cross-sectional area and average diameter of the suspended bubbles decrease with depth, so the acoustic environment favors multiple scattering, with detectable returns coming from a range of depths. Thus we expect differences between our first return and last valid return when the target is a layer of suspended bubbles beneath a field of wind-generated surface waves.

[19] For our case, once the water column has cooled to the freezing point in winter, episodes of high winds and low air temperatures are expected to generate frazil ice crystals in the water column. Qualitative field observations by SM show that the presence of frazil and grease ice on the surface damps out the surface waves and suppresses but does not eliminate wave breaking, which should inhibit bubble generation. In the following, because we do not know the acoustic properties of frazil and we do not know if acoustically significant amounts of air bubbles are suspended during frazil events, we cannot say whether ULS observations of deep scatterers in winter are from frazil crystals, air bubbles or from a combination of both. We will show, however, that the occurrence of deep scatterers is correlated with the Langmuir circulation, and with episodes of the water column cooling to the freezing point or even becoming supercooled. Although our observations are consistent with frazil formation at depth, we cannot eliminate air bubbles as possible scattering sources.

3. Comparison of the Meteorological, SAR and ULS Data

[20] We next summarize the SAR observations of frazil polynyas, describe the meteorological data, and compare ULS observations of deep scattering with the meteorological data and SAR observations.

3.1. SAR Observations of Polynyas

[21] For Days 6–90, Figure 2 shows a sequence of 14 SAR images that include all available frazil polynya imagery within the period. We identify polynyas from the presence of the Langmuir-generated bright linear streaks, which we call active frazil. We describe the frazil polynyas by the notation

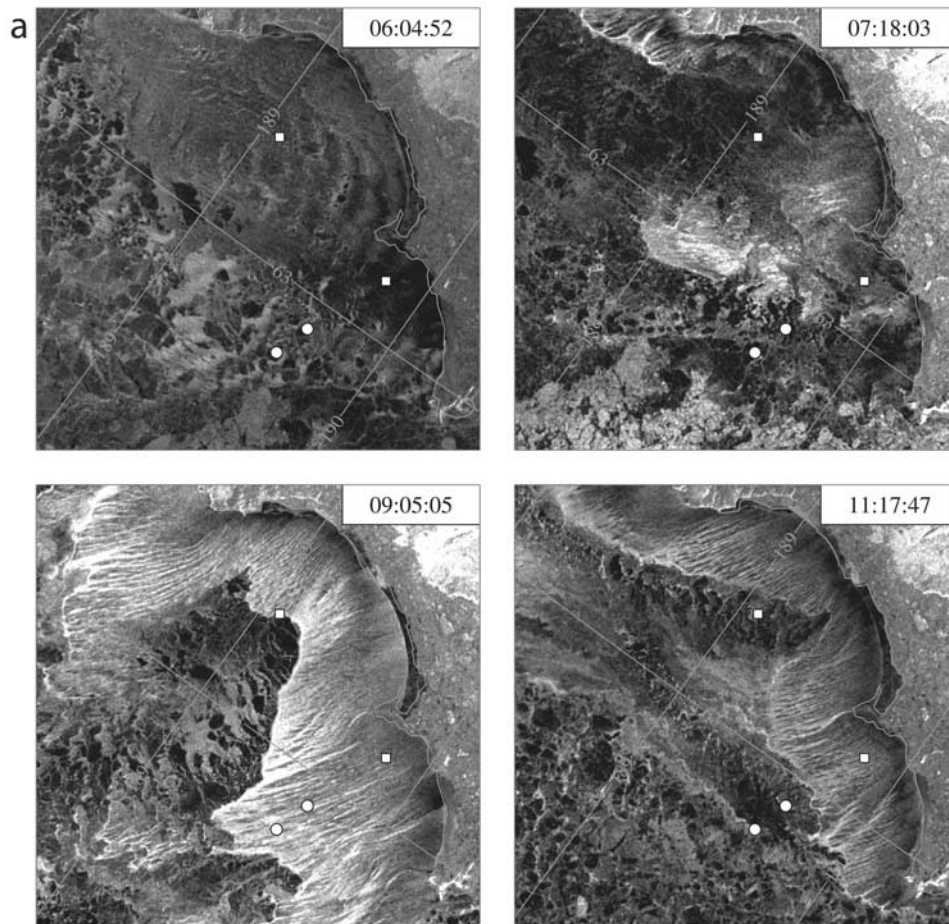


Figure 2. SAR imagery of frazil ice polynyas for Days 6 through 90. On each image, the circles show the ULS positions; the squares, the SeaBird positions. The images are identified by their acquisition time given as day: hour: minute. (a) Days 6, 7, 9, 11. (b) Days 44, 45, 52, 55, 78, 79. (c) Days 85, 86, 88, 90 (SAR images copyright 1999 by the Canadian Space Agency).

FP1, FP2, through FP5. In addition, between Days 32 and 37, which was a period of weak very cold offshore winds, we observed the formation of a primarily congelation ice polynya that we call CP1 and discuss later. The first frazil polynya, FP1, occurs during Days 6–15. Figure 2a shows that on Day 6, the active frazil is confined to a small active region off Southwest Cape, with a mixture of open water and thin ice above and adjacent to the ULSs. On Day 7, there is an additional active frazil region south of the Kookooligit Mountains, and by Day 9, the polynya is very large, such that active frazil occurs over both ULS moorings. On Day 11, the polynya is reduced in size.

[22] The second frazil polynya FP2 occurs during Days 44 and 45 (Figure 2b). The Day 44 image shows only a small polynya off Southwest Cape; Day 45 shows that the polynya has grown such that a mixture of accumulated frazil and large floes cover the two ULSs. For the third frazil polynya FP3, Days 52 and 55 show that although a polynya occurs, the active frazil does not extend over the ULSs, but covers the two nearshore SeaBirds. For the fourth frazil polynya FP4 on Days 78 and 79, Day 78 shows that ULS-15 is at the boundary between the active and accumulated frazil, while ULS-42 is under a mixture of accumulated

frazil and large floes, and Day 79 shows that only the P2 mooring is under active frazil, while ULS-15 is under accumulated frazil. Finally, the SAR images for Days 85, 86, 88 and 90 show the fifth frazil polynya FP5, which on Day 85 is so large that all of the moorings appear to be under active frazil. On Day 86, ULS-15 and the two SeaBirds appear to be under active frazil; on Day 88, both ULSs are under thin ice and the SeaBirds are under active frazil; on Day 90, ULS-15 appears to be under accumulated frazil and close to the active region. The next subsection compares these observations with the meteorological observations and with ULS observations of deep scatterers; section 6 tests the Pease model using the SAR images and ULS ice thicknesses for Days 45, 78, 79 and 90.

3.2. Comparison of the Meteorological Data With the ULS Observations

[23] The meteorological data consists of the gridded NCEP (National Center for Environmental Prediction) sea level pressure and the air temperature T_A calculated on the NCEP grid using optimal interpolation of the air temperatures measured at the surrounding Russian and US land stations. The geostrophic wind speed U_G is calculated from

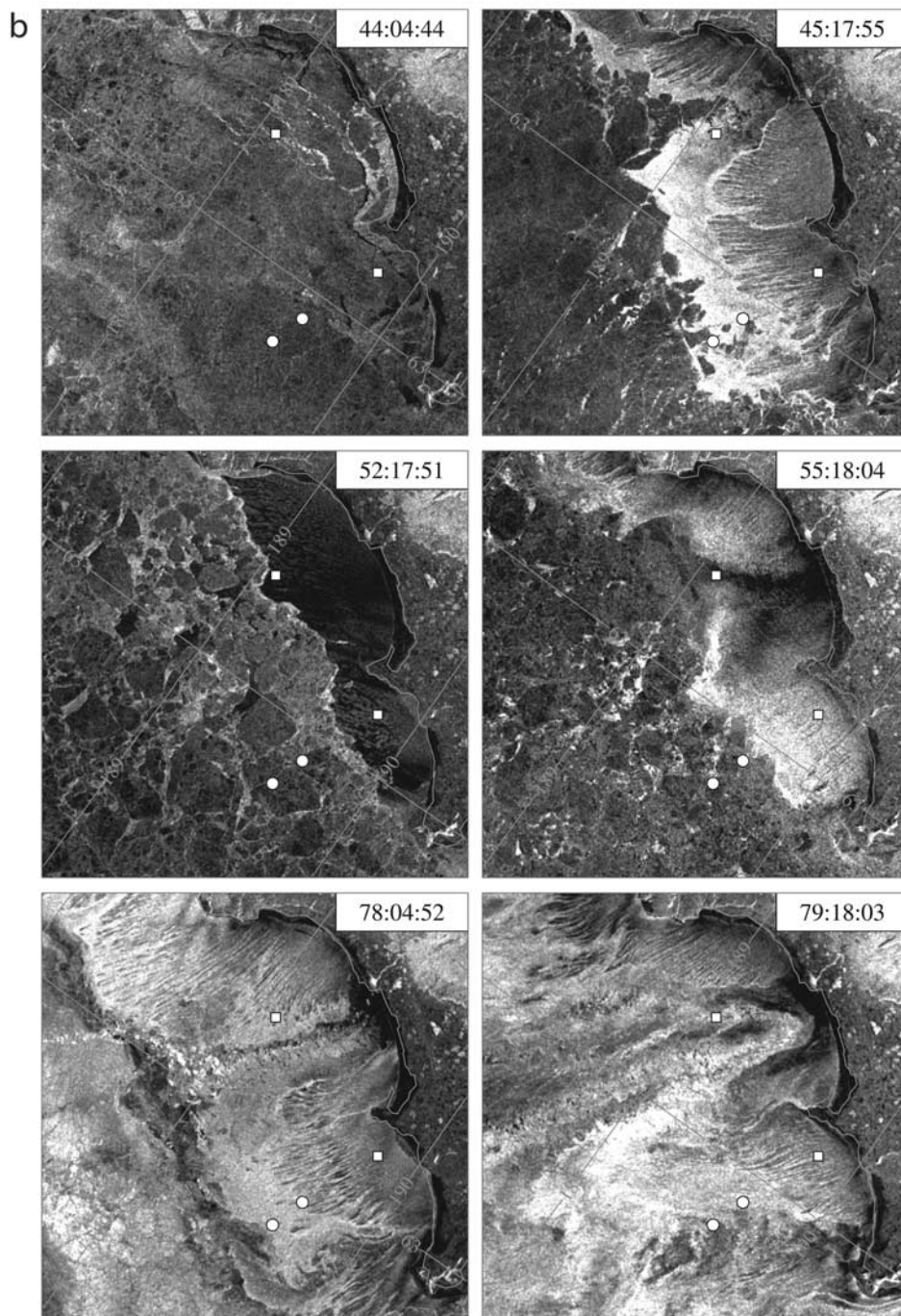


Figure 2. (continued)

the gridded NCEP 6-hour pressure fields. Because this wind field ignores the influence of the topography on St. Lawrence Island, as *Walter* [1989] shows from his aircraft meteorological flights, the actual airflow around the mountains and south of the island is more complicated.

[24] For the first 90 days of 1999, Figure 3 compares the 6-hour time series of geostrophic wind and air temperature for a point in the polynya region with the 6-hour averages of the first and last valid returns from the two ULSS. The labeled horizontal bars under Figure 3c show the approximate time periods corresponding to the different polynya

events discussed in the previous section, the letters and numbers under the bars identify the events, and the vertical lines extending through the figures show their duration.

[25] Figure 3a shows the geostrophic wind direction and magnitude; Figure 3b shows the 10-m air temperature. Geostrophic winds are used because at least in the high Arctic and under free drift conditions, the ice drift is approximately in the geostrophic wind direction [*Overland and Colony*, 1994]. Because the ice south of the island is adjacent to an open boundary, it will have a small internal ice stress such that the free drift relation should be approx-

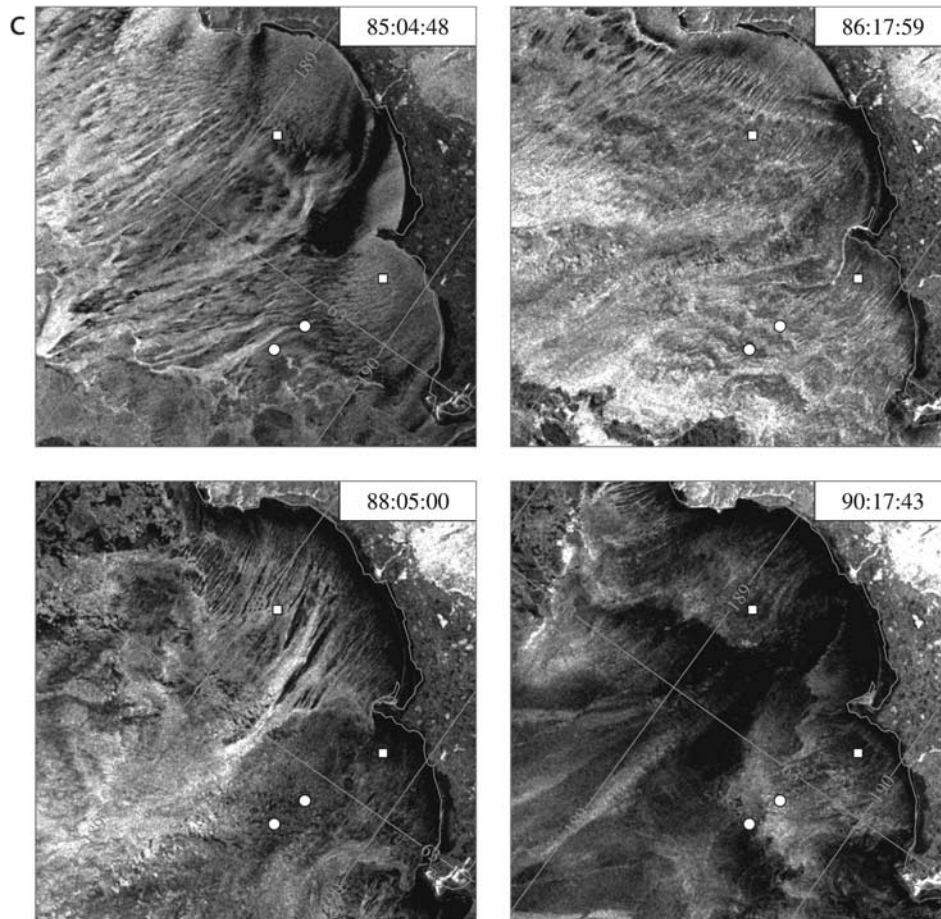


Figure 2. (continued)

imately correct. During the FP events, the figure shows that the winds are from the northeast quadrant with velocities exceeding 20 m s^{-1} , and that the air temperatures are generally greater than -20°C . Because for FP2 or Days 44–45, the geostrophic wind directions are such that a polynya should not form, the existence of a polynya suggests that the geostrophic winds are modified by the topography such that the surface winds are offshore. In contrast and during CP1, the wind speed is less than 10 m s^{-1} and the majority of the air temperatures are below -30°C , so that except in the immediate vicinity of the island, the polynya consists of congelation ice being advected offshore.

[26] Figures 3c and 3d show the 6-hour averages of the 5-min first return (upper line) and last valid return (lower line) for the two ULSs. The difference between the two time series is darkened; this occurs when the first and last valid returns diverge from one another and implies the presence of deep scattering. Consistent with the SAR observations, the deepest scattering occurs during FP1 and FP5, with shallower scattering at FP4 and possibly FP2 and FP3. In contrast, CP1 shows only thin ice. Also, the scatterers at ULS-15 occur at significantly greater depths than those at the offshore ULS-42. Even if we divide the response at ULS-15 by a factor of two, this instrument still observes deeper scatterers.

[27] Comparison of the winds, ULS returns and SAR observations show that scatterers occur in the water column during periods of strong offshore winds and when the SAR

observes frazil events. For the FP1 event, the two peaks in the ULS-15 thicknesses correspond to the two peaks in the wind magnitude. The other scattering events also occur around wind maxima. The congelation polynya event, CP1, occurs during a period of relatively weak winds and very low temperatures. For this case, the ice was slowly advected offshore, such that only congelation ice occurred over the ULSs. For FP1 and CP1, we have ULS, AVHRR and SAR data; for FP2 through FP5, we have only ULS and SAR data. The FP1 and CP1 polynyas thus provide our best opportunity for the comparison of the ULS and satellite ice thicknesses.

4. Satellite Estimates of Ice Thickness

[28] In the following, section 4.1 describes our technique for estimation of the ice thickness from the combination of the meteorological and AVHRR data, and section 4.2 derives the error bars on this estimate. Section 4.3 then presents images of the AVHRR-derived ice thicknesses superimposed on nearly-coincident SAR images that show the spatial distribution of ice thickness for the FP1 and CP1 polynyas.

4.1. Estimation of the Ice Thickness From AVHRR Data

[29] Our model for estimation of the ice thickness follows *Yu and Rothrock* [1996], in that we assume the ice is thin,

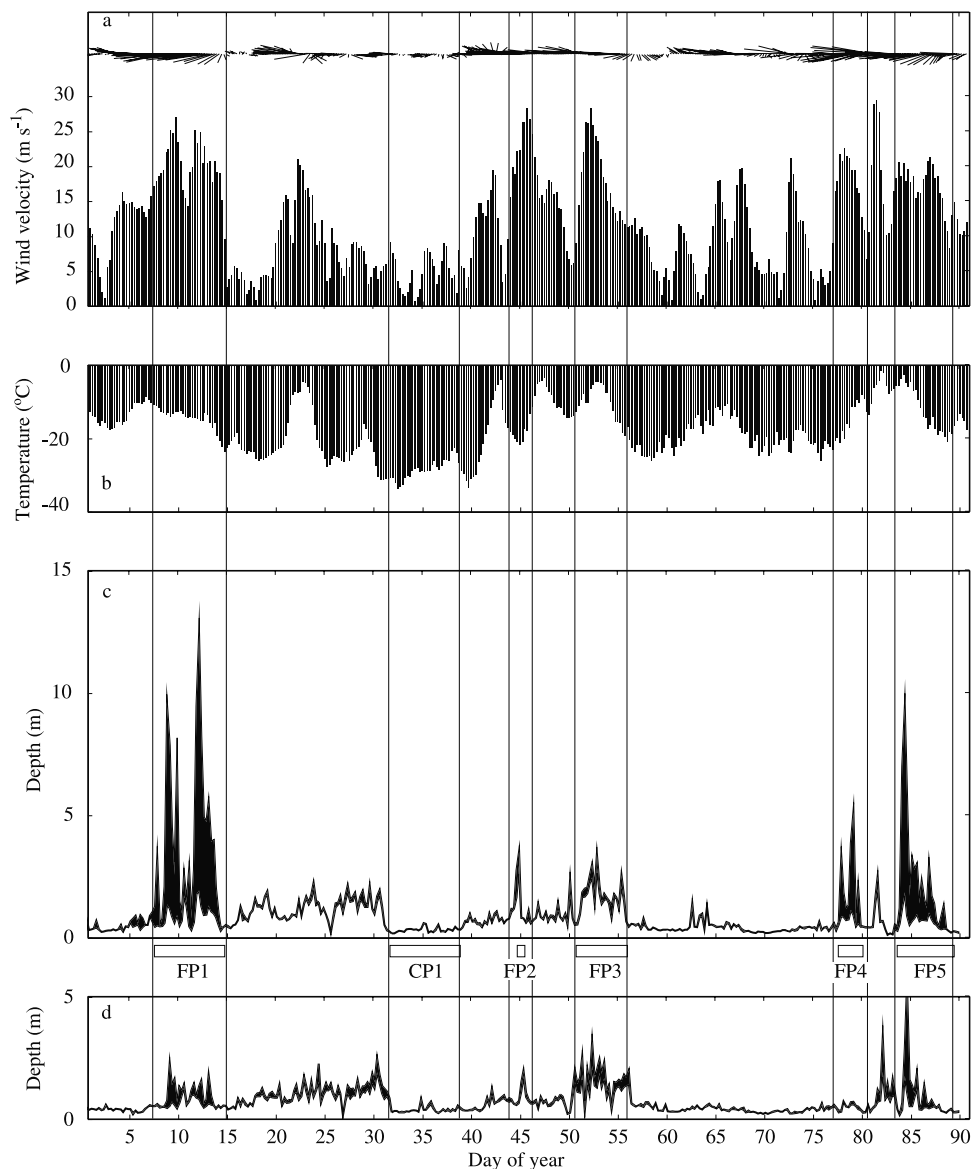


Figure 3. Comparison of the 6-hour time series of geostrophic wind velocity and direction and the 10-m air temperature at 62.71°N and 170.54°W in the polynya region south of the island with the 6-hour averages of the 5-min returns from ULS-15 and ULS-42. (a) Geostrophic wind direction and magnitude, where the wind is in the direction shown by the stick plot. (b) Air temperature. (c) The 6-hour averages of the first and last valid thicknesses at ULS-15. (d) Averages at ULS-42. See text for additional information.

the water temperature is constant at -1.8°C , and the temperature profile is linear within the ice. We then set the heat flux through the ice equal to the atmospheric flux, which allows us to solve for what we call the thermal ice thickness h_T . According to *Yu and Rothrock* [1996], this linear approximation is valid for ice thicknesses less than about 0.5 m.

[30] The inputs to the atmospheric heat flux algorithm are the AVHRR ice surface temperature T_S , the 10-m air temperature T_A and the 10-m wind speed U , where all values are either measured at a geographic location corresponding to an AVHRR pixel location, or interpolated to this point. The surface temperature T_S is derived from the 11 and 12 mm

AVHRR channels, using the algorithm of *Key and Haefliger* [1992] and *Key et al.* [1997], where through use of channel pairs, the atmospheric absorption and emission due to water vapor are removed. The retrieved temperature T_S has a resolution of about 1 km, corresponding to the size of the AVHRR pixel, and a spatial location accuracy also of about 1 km. The 10-m wind speed U is calculated from the geostrophic wind speed U_G through application of a reduction factor of 0.70, and a rotation of 33° to the right [*Overland and Colony*, 1994]. The air temperatures T_A are calculated on the NCEP grid using optimal interpolation of the air temperatures measured at the surrounding Russian and US land stations, then reinterpolated to a 1-km grid in the region of interest.

[31] Following *Martin et al.* [1998], the total heat flux F_T received from the upper hemisphere at the surface can be written as

$$F_T = F_S + F_L + F_E + F_D, \quad (3)$$

where F_S is the sensible heat flux, F_L is the latent, F_E is the emitted longwave, and F_D is the downwelling longwave. Equation (3) includes all terms except the incident solar radiation, which we discuss below. In equation (3), the sensible and latent heat fluxes are calculated using bulk coefficients, the emitted longwave radiation is based on the surface temperature, and the downwelling longwave is a function of the air temperature and the cloudiness. Since the surface must be visible to the satellite for these measurements to occur, we assume cloud-free conditions.

[32] One problem that we encountered with this approach was how to deal with the incident solar radiation. For ice without snow cover, *Grenfell and Maykut* [1977] discuss the albedo and transmission properties of sea ice. They show that at the interface, part of the incident solar radiation is absorbed, part is reflected, and part is transmitted, where depending on the radiation wavelength and the ice thickness, the transmitted radiation is partially absorbed in the ice interior. They also show that these properties have a strong dependence on wavelength, where the ice is transmissive at the short, blue wavelengths, then becomes increasingly absorptive as the wavelength increases. Because of our uncertainty as to the partitioning of the solar radiation, we restrict our analysis to solar zenith angles greater than 75° , for which the absorbed and transmitted solar fluxes make negligible contributions to equation (3), where this restriction includes the nighttime case when the zenith angle exceeds 90° .

[33] At the surface, we assume that the conductive heat flux through the ice F_{ice} , is a linear function of the temperature difference across the ice,

$$F_{ice} = k_i(T_S - T_0)/h_T, \quad (4)$$

where $k_i = 2.03 \text{ W m}^{-1} \text{ }^\circ\text{K}^{-1}$ is the conductivity of sea ice, T_0 is the seawater temperature, assumed constant at -1.8°C and h_T is the derived ice thickness. As long as the ice-air interface is not melting and is free of snow, energy balance at the interface requires that $F_{ice} = F_T$, so we can solve equation (4) for h_T as follows:

$$h_T = k_i(T_S - T_0)/F_T. \quad (5)$$

This equation defines our AVHRR retrieval of ice thickness, which we call the thermal ice thickness.

4.2. Errors in the Ice Thickness Retrieval

[34] The error in the retrieved ice thickness h_T is based on uncertainties in the following variables: the AVHRR-derived ice surface temperature; the gridded air temperature, the surface wind speed, the longwave heat balance, and for comparison with the ULS observations, the geolocation error in the AVHRR pixels relative to the ULS locations. Because h_T is a nonlinear function of T_S and F_T , where F_T is itself a nonlinear function of T_S , T_A and U , we estimate the error on h_T using the following Monte Carlo simulation. First, we assume that the errors in the three input variables

T_S , T_A and U are normally distributed and independent, where we neglect the weak dependence of the geostrophic wind on density through T_A . Second, we assume that the uncertainty or standard deviations of the input variables are as follows: $\Delta T_S, \pm 1^\circ\text{C}$; $\Delta T_A, \pm 2^\circ\text{C}$; $\Delta U, \pm 1 \text{ m s}^{-1}$.

[35] Third, to account for geolocation error, we perform the Monte Carlo simulation in a 3×3 pixel square around the grid point assumed to contain the ULS mooring, where the area of each pixel is 1 km^2 . Assuming a uniform ice drift, this 3×3 square also accounts for errors due to the difference between the AVHRR acquisition time and the ULS observation interval. For each of the nine AVHRR observations around the mooring locations, a population of $M = 1000$ observations is simulated by construction of three normally distributed random vectors with means set to the observed values T_S , T_A and U , and standard deviations set to the assumed observational uncertainties ΔT_S , ΔT_A and ΔU . We then calculate the ice thickness $h_T = h_T(T_S, T_A, U)$ for each of the 9000 simulated observations. Error bars are drawn from the 16th to the 84th percentile of h_T , so that each error bar contains 68% of the Monte Carlo population, analogous to the 1 standard deviation that would occur for a Gaussian distribution. Since the distribution of h_T is asymmetric, neither the mean nor the observed value of h_T will generally lie at the center of the error distribution.

4.3. Examples of Satellite Thickness Observations

[36] Figures 4a and 4b are composite images of the polynya region constructed from near-simultaneous SAR and AVHRR for FP1 during Day 9 (January 9) and for CP1 during Days 31, 33, 35 and 37 (January 31, February 2, 4, 6). For each composite, the color corresponds to the thermal ice thickness h_T ; the value or light-dark content is from the corresponding 200-m resolution SAR image.

[37] For FP1, Figure 4a shows that the two ULSs are in an active frazil region. The thermal thicknesses at ULS-15 and ULS-42 are respectively 7 and 8 mm; while the 6-hour averages for the ULS first returns are respectively 7 and 2 m; for the ULS last valid returns, 1.1 and 0.6 m. Although under conditions of active frazil, the last valid return may represent the bottom of the surface frazil accumulation, we have no way of verifying this. The figure shows that within the polynya, the thermal ice thickness increases away from the coast, while the ULS first returns show a thickness decrease with distance from the coast that is much greater than the factor-of-two difference associated with the autumn and summer scattering. The reason for the large difference between the ULS and thermal thicknesses is that the frazil ice is a slurry with a relatively warm surface and with its crystals distributed at depth by the Langmuir circulation. Moving away from the coast, the wave damping increases, so that the Langmuir circulation should decrease such that there is less frazil at depth, while the downwind advection causes the near-surface thickness to increase. Although the AVHRR and ULS observations give different results, they are consistent with the frazil behavior. For comparison with the thicknesses within the polynya, we calculate the ice thickness using a $3 \text{ km} \times 3 \text{ km}$ AVHRR surface temperature estimate. From this, the ice thickness north of the island is 40 cm, and in the pack ice south of the island and surrounding the polynya region of new ice growth, about 10–12 cm. In the ice surrounding the active frazil region, the ice thickness is 4–6 cm.

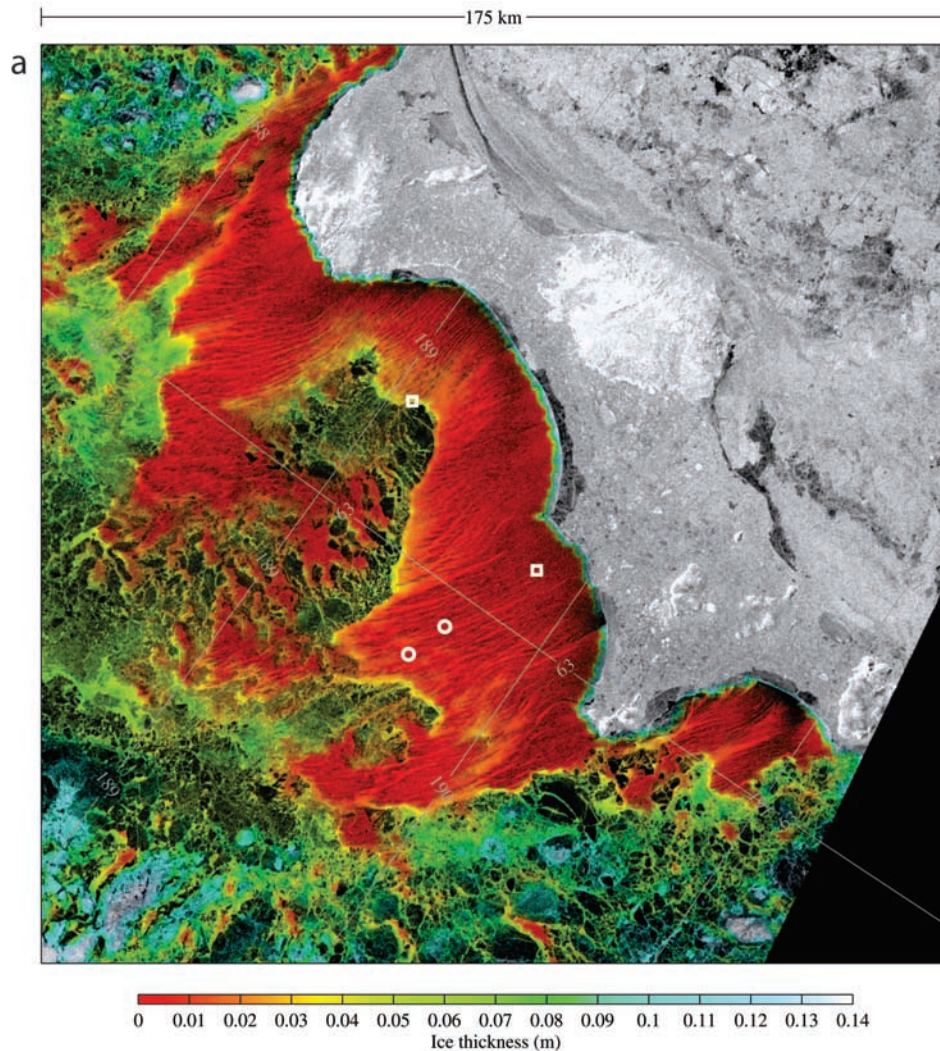


Figure 4. Composite SAR and AVHRR images of the St. Lawrence Island polynya. The colors correspond to the thermal or AVHRR thicknesses; the texture and detail correspond to the SAR. The circles show the ULS positions; the squares show the SeaBird positions. (a) Day 9. The SAR image was acquired at 0504 UT and the AVHRR image at 0431, so the two images are 33 min apart. (b) Days 31, 33, 35 and 37. Figures 4a and 4b have different color scales. On Day 31, the SAR was acquired at 1803 UT, the AVHRR at 1829 UT; on Day 33, SAR was acquired at 0504 UT, AVHRR at 0359 UT; Day 35, SAR was acquired at 1747 UT, AVHRR at 1840 UT; Day 37, SAR was acquired at 0447 UT; AVHRR at 0411 UT (SAR images copyright 1999 by the Canadian Space Agency).

[38] Using a different color scale, Figure 4b shows four similar composite images for Days 31, 33, 35 and 37 during CP1, when the winds are much weaker and the air is much colder. During this period, most of the ice in the images has a thermal thickness greater than 0.3 m, except in the large green area of new ice formation south of the island, and in a narrow region immediately adjacent to the island. For this period, the next section compares the ULS and thermal ice thicknesses.

5. Comparison of the Thermal and ULS Ice Thicknesses

[39] During CP1 and for Days 26–41, Figures 5a and 5b compare the 5-min samples of the ULS last valid return thicknesses with the thermal thicknesses. In the figure, the

small black dots are the 5-min ULS samples; the open circles and vertical lines with crossbars are the thermal thicknesses and uncertainties, where the crossbars correspond to the 16th through 84th percentiles of the Monte Carlo distributions. For Days 30–38, which is during the period when ice is being exported away from the island, the figures show that the ULS ice thicknesses cluster around modal values between 0.2 and 0.3 m, with a spread of points around the mode and a number of intermittent larger thicknesses. For ULS-15, the spread of the modal values is about ± 2 cm; for ULS-42, about ± 4 cm. The larger ULS-42 uncertainty is probably due to the small water bubble in the acoustic lens, which slightly defocused the beam.

[40] For the same period, both the ULS modal and the thermal thicknesses exhibit fluctuations with a period of

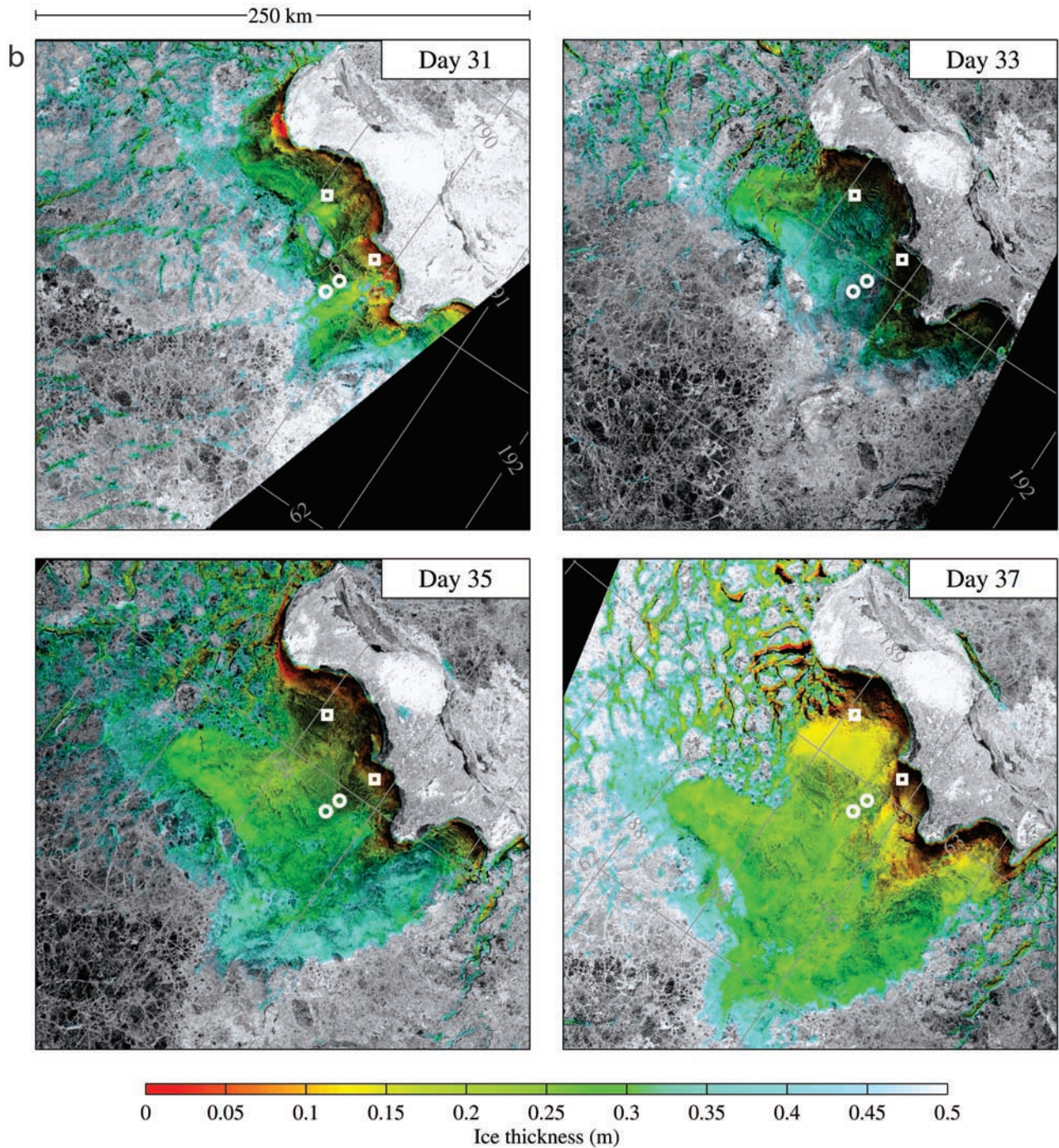


Figure 4. (continued)

approximately 4 days. Phase differences between the extrema of these fluctuations at the two ULS moorings are less than four hours, with an indication that some of the fluctuations at ULS-15 precede those at ULS-42. Ice initially located at ULS-15 would have to move at speeds in excess of 0.8 m s^{-1} to reach ULS-42 within 3 hours. Because tracking of specific floes in the SAR images on Days 31 to 37 shows that the observed offshore ice drift rate is $12\text{--}15 \text{ km d}^{-1}$ or about 0.15 m s^{-1} , this is not the cause of these phase differences. Alternatively, it might be

that the component of ice velocity perpendicular to the line between the two ULS moorings was advecting thickness variations past both sensors at approximately the same time. Examination of other environmental quantities that might possibly affect errors in the ULS thickness estimates, including sea level pressure, water temperature, water salinity, current speed and ULS depth, revealed no obvious correspondences with the thickness fluctuations. The qualitative agreement between the changes in ULS thickness and thermal thickness leads us to believe that these fluctua-

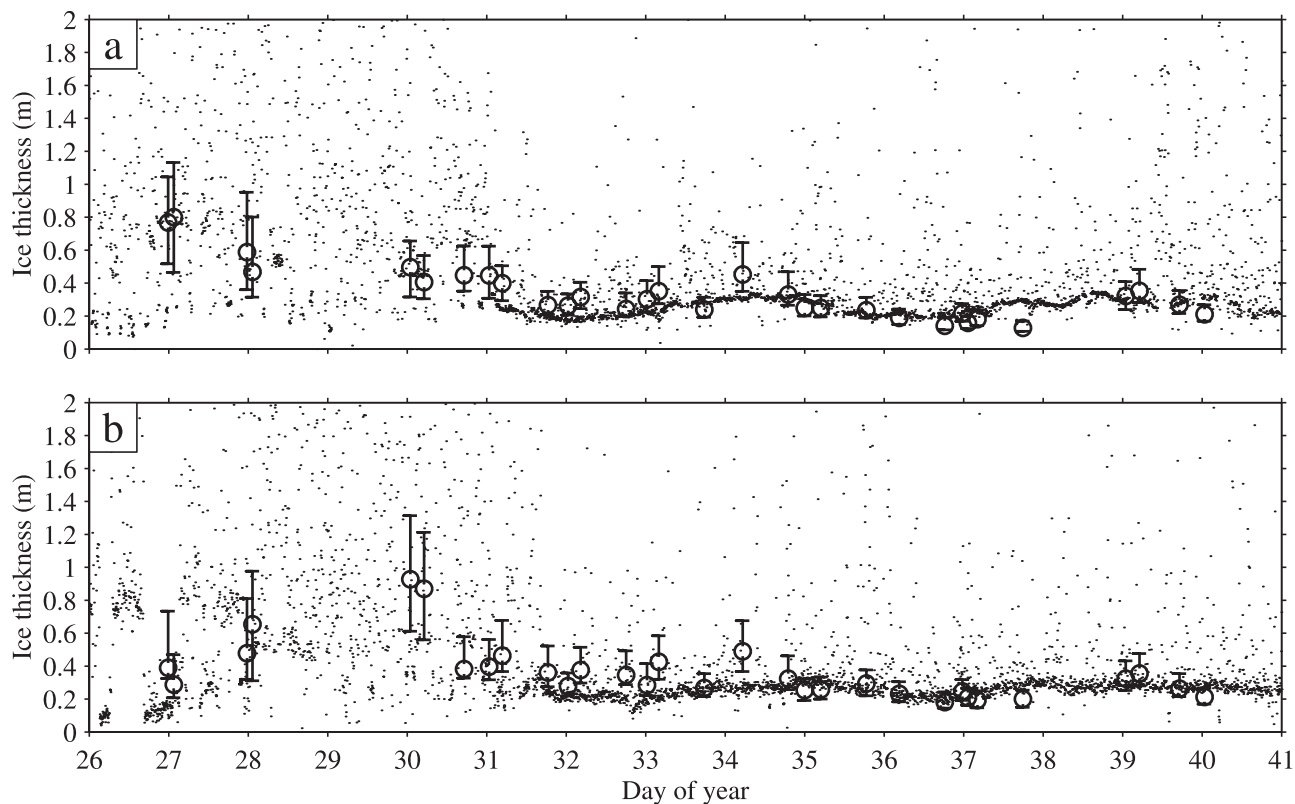


Figure 5. Comparison of the thermal and 5-min ULS ice thicknesses for Days 26–41. The dots show the 5-min ULS samples; the open circles are the thermal thicknesses and the vertical lines with crossbars give the range of the uncertainties. (a) ULS-15; (b) ULS-42. See text for further description.

tions really do reflect ice thickness, although we lack a definitive explanation.

[41] For the three periods in which we have coincident data, Figure 6 compares all of our thermal ice thicknesses with the mean and mode of the ULS 5-min last valid return thicknesses grouped into 6-hour blocks. For each block, the mode is the center thickness of the largest bin in a 5-cm resolution histogram. If two equally sized bins exist in the histogram, the mode is chosen as the smaller of the two thicknesses. In the figure, the ULS mean is the upper continuous line; the mode is the lower. The small bar in the middle of Figure 6a shows the error associated with the ULS observations. Our choice of 6 hours as an averaging period is based on Days 31–40, when the ice drifted offshore at a rate of $12\text{--}15\text{ km d}^{-1}$, or $3\text{--}4\text{ km}$ in a 6-hour interval. Since our AVHRR sample area measures $3 \times 3\text{ km}^2$, this means that for at least Days 31–40, the length scales of the ULS and AVHRR averages are similar.

[42] Comparison of the first set of panels for Days 7–12 or polynya event FP1 show that the ULS mean and mode are much larger and have greater fluctuations than the thermal estimates. In contrast, the thermal thicknesses are at most a few centimeters. This shows that during periods of strong frazil formation the ULS thicknesses are very large, while the thermal thicknesses are of order mm. Because the surface frazil ice consists of a slurry, there is no thickness consistent with the estimates of both instruments. The quantity most directly related to the surface heat budget is the ice mass per-unit-area integrated over the column, which

neither instrument provides. Both the ULS and AVHRR produce results consistent with the Langmuir circulation and with the transport of frazil crystals to depth; the AVHRR observes a warm slurry surface temperature and thin ice, the ULS observes deeper scatterers.

[43] The middle set of figures compares the thicknesses for Days 26–41, which is the same CPI period shown in Figures 4b and 5. For Days 26–31, Figure 5 along with examination of the high-frequency data shows that the ice is ridged, with many keels of depths of $1\text{--}2\text{ m}$. For the same period, the middle set of panels in Figure 6 shows that the thermal thicknesses either agree with the mode or lie between the mode and mean, which is what we would expect for ridged ice. Toward the end of this period on about Day 31, as Figure 4b shows, the winds move the thicker ice offshore to be replaced by flatter congelation ice. As the ridging within the AVHRR and ULS fields-of-view decreases, Figure 6 shows that the mean and the mode converge and the thermal and ULS estimates generally agree within their respective uncertainties. For Days 32–38, Figure 5 shows that the ice is nearly level, with only a few small keels. On Day 39, the winds reverse so that the ice becomes ridged, and the mode and mean again diverge. This period of very cold, weak offshore winds yields our best agreement between the ULS and AVHRR ice observations.

[44] The third set of panels in Figure 6 shows the comparison for Days 56–77. This period had very few clear days, as well as a higher sun angle, so that it contained less usable data than in earlier periods. With one or two

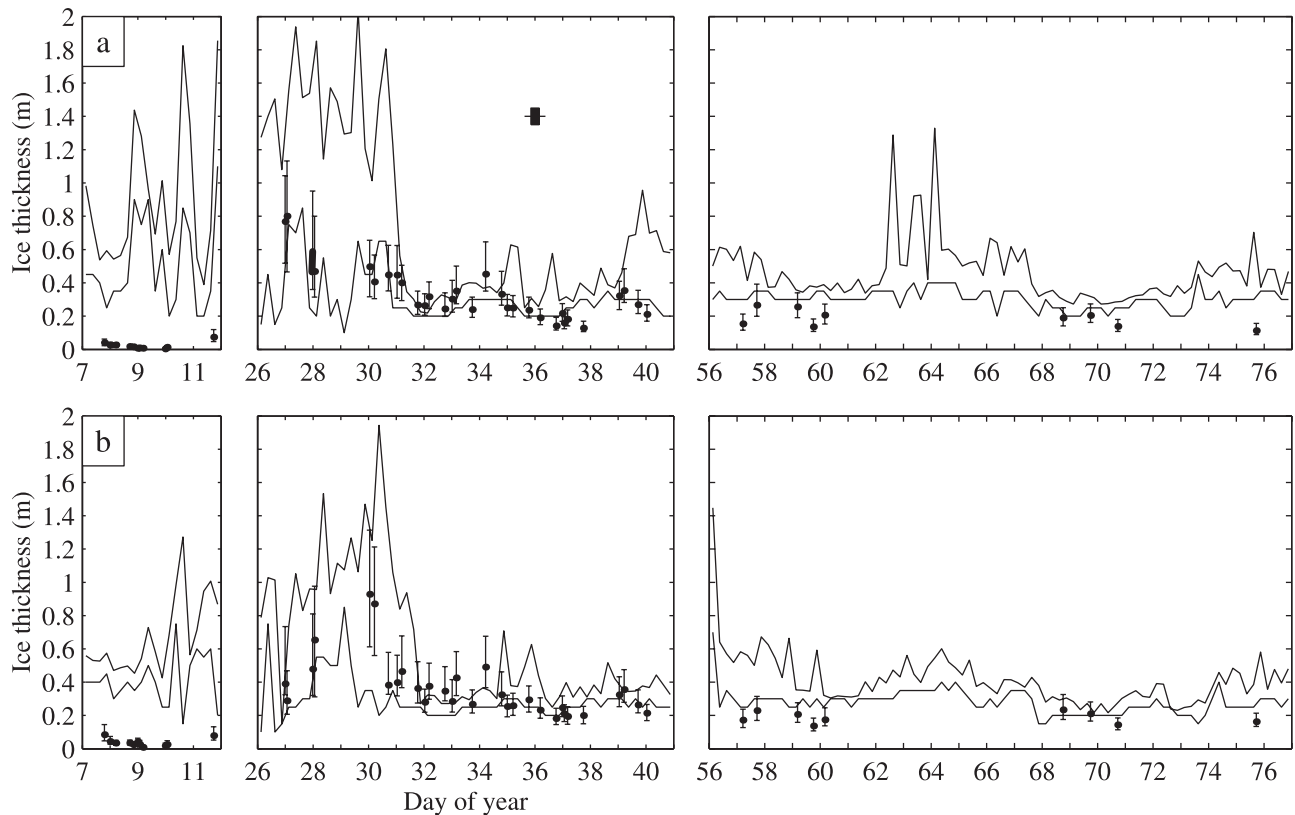


Figure 6. Comparison of the ULS and thermal ice thicknesses at (a) ULS-15 and (b) ULS-42, for Days 7–12, 26–41 and 56–77, where only periods of coincident data are shown. The continuous black lines show the 6-hour mean (upper) and mode (lower) of the ice thicknesses derived from the ULS last valid return. The dots and vertical lines with crossbars show the thermal thicknesses and uncertainties. The error bar in the upper middle panel shows the ULS RMS uncertainty. See text for further description.

exceptions on Days 59 and 75, the thermal thicknesses lie either on the mode or slightly below it. The reason for the exceptions, and possibly for the low bias of the AVHRR estimates, may be due to the presence of thin warm clouds. We discovered this from a comparison of AVHRR images acquired during daytime at times close to the nighttime images used in the analysis. From these daytime images, examination of the near-infrared channel 2 and the thermal-infrared channel 4 images showed the presence of thin transparent clouds that are warmer than the ice surface and which are barely visible in the channel 4 images. These clouds are apparently the cause of the outliers and may also be associated with the approach of spring, since the January and February clouds are generally much colder than the ice. In summary, Figure 6 suggests that for thin congelation ice with only a few pressure ridges per unit area, the thermal and ULS thicknesses agree within their error bars. The discussion also shows that the algorithm works best under cold winter conditions and gives inaccurate results in the presence of thin clouds.

6. Comparison With the Pease Model

[45] Combination of the SAR and AVHRR imagery with the ULS observations means that for several of the SAR images, we can retrieve all of the variables in equation (1) and compare the observed and calculated polynya widths.

In each case, we measure the polynya width from the SAR image, offshore ice advection from pairs of SAR images, the heat flux from the meteorological data and the frazil accumulation thickness from either AVHRR or ULS data, where we reduce the measured frazil thicknesses to solid ice thicknesses following *Martin and Kaufman* [1981]. In this calculation, we derive the accumulation thickness from the AVHRR for two clear days, Day 9 and Day 35, and from the ULS for 4 cloudy days, Days 45, 78, 79 and 90.

[46] Beginning with Day 9, we calculate the ice advection from examination of the SAR images for Days 7 and 9. Because there are several floes common to both images, from their displacement between images, we calculate a pack ice velocity of about 0.45 m s^{-1} . At the time of the Day 9 image, the 10-m air temperature T_A is -14°C and the 10-m wind speed U is 18 m s^{-1} , where the wind direction is approximately parallel to the frazil streaks. The heat loss from the active frazil is 500 W m^{-2} or in terms of ice growth, $1.6 \times 10^{-6} \text{ m s}^{-1}$ or 14 cm d^{-1} . In this calculation, we use the fresh water latent heat of freezing $L = 334 \text{ kJ kg}^{-1}$. The AVHRR retrieved thickness of the accumulated frazil ice surrounding the active frazil is 4–6 cm. Use of the *Martin and Kaufman* [1981] result that frazil ice consists of 40% ice crystals yields $h_C = 2\text{--}3 \text{ cm}$. From the SAR image, the observed polynya width is between 35 and 50 km. Substitution of the observed heat flux, ice drift and h_C into

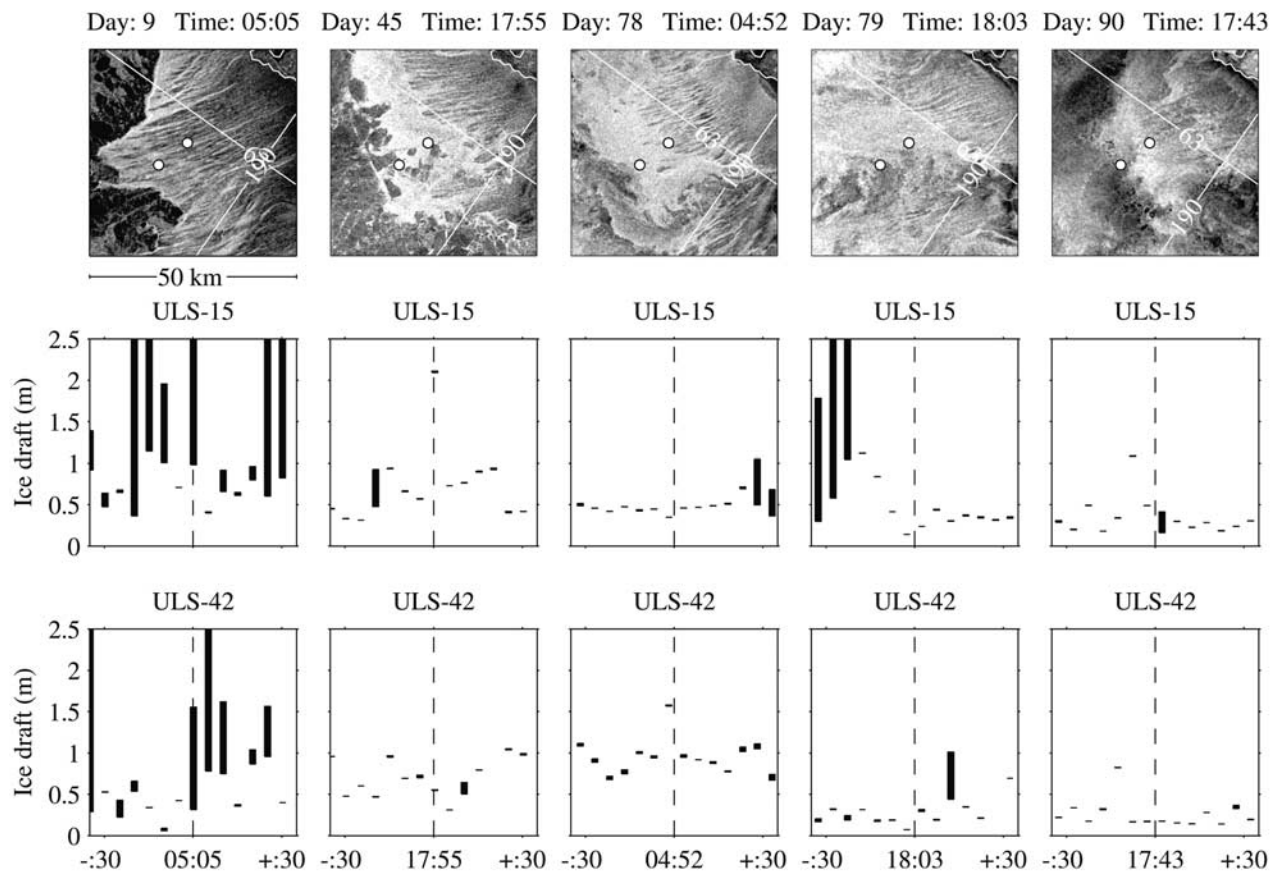


Figure 7. SAR images and measured ice drafts at ULS-15 and ULS-42 for five events. On the SAR images, the white circles show the ULS locations. On the ULS figures, the vertical dashed lines mark the SAR acquisition time t_{SAR} ; the bars and horizontal lines show the 5-min ULS averages of the first and last valid return ice drafts for ± 30 min from the SAR acquisition time. When the ice draft is shown as horizontal line, the first and last valid return are equal; when it is shown as a vertical bar; the two responses differ where the bar shows their range.

equation (1) gives a theoretical width of $R = 4\text{--}6$ km or much smaller than the observed. Because the winds accelerate between Days 7 and 9, the lack of agreement may indicate that the polynya has not reached steady state, or alternatively that the accumulated frazil ice is not completely frozen with depth.

[47] The second AVHRR comparison is for Day 35, when a 4–5 km wide frazil polynya is visible in the SAR image off Southwest Cape. For this day, $T_A = -29^\circ\text{C}$ and $U = 5.5$ m s⁻¹, where the winds are offshore. Even though these winds are weaker and colder than the previous case, the heat loss in the frazil region is 500 W m⁻² or approximately equal to the previous case. The surface wind speed exceeds the 5 m s⁻¹ threshold velocity for the onset of polynya formation [Pease, 1987; Winsor and Björk, 2000]. From calculation of the floe velocities between Days 33 and 37, the average pack ice velocity is 0.21 m s⁻¹. For Day 35, the AVHRR thicknesses of the accumulated frazil ice downwind of the Southwest Cape polynya are 4–7 cm, yielding $h_C = 2\text{--}3$ cm, where the larger values occur farther from the edge of the active frazil. Substitution of the ice drift, the heat flux and the accumulation depth into equation (1) gives $R = 2\text{--}3$ km, or slightly less than the observed.

[48] The next set of comparisons uses SAR and ULS observations. For Days 9, 45, 78, 79 and 90, Figure 7 shows the SAR images in the vicinity of the ULSs and the ULS data acquired within ± 30 min of the SAR acquisition time t_{SAR} . The ULS plots show the vertical range of the 5 min first and last valid returns. For Day 9, which is included for comparison, the SAR image shows that the ULSs are under frazil plumes, and the ULS data again show the large differences between the first and last valid returns characteristic of deep scatterers. For the other days, the SAR images show that in each case ULS-15 appears to be beneath accumulated frazil ice, although on Day 45, the return is complicated by the presence of an adjacent large floe.

[49] Table 2 lists the SAR images used in this calculation and the ice velocity U_I calculated from the image pairs. Calculation of the parameters used in equation (1) is done for Day 45, Days 78 and 79, where the ice drift for both days is calculated from the same image pair, and Day 90. The table also lists U , T_A and the heat flux taken from the 6-hour observation closest to t_{SAR} , where the flux is given both in terms of W m⁻² and in m s⁻¹ units of ice growth. The seventh column lists the accumulated frazil ice draft observed at ULS-15 in the Figure 7 data. For Days 78, 79

Table 2. Comparison of the Observed Polynya Properties With the Pease Model^a

Day of Year	U_i , ms^{-1}	U_r , ms^{-1}	T_A , $^{\circ}\text{C}$	Heat Flux, W m^{-2}	Ice Growth, $\text{m s}^{-1} \times 10^{-6}$	Ice Draft, m	h_C , m	Polynya Widths	
								Obs., km	Calc., km
44–45	0.32	20	−18	690	2.3	0.5 ± 0.2	0.2 ± 0.1	20–25	30 ± 15
78–79	0.36	15	−20	600	2.0	0.45 ± 0.05	0.2 ± 0.02	25–30	36 ± 4
78–79	0.36	11	−11	245	0.8	0.35 ± 0.05	0.15 ± 0.02	17–23	70 ± 10
88–90	0.14	8	−18	300	1.0	0.25 ± 0.05	0.1 ± 0.02	15–19	15 ± 3

^aThe SAR images corresponding to the pairs of days are used in the derivation of the ice drift U_i ; the day in boldface is used for calculation of the polynya width and the other variables. See text for further discussion.

and 90, where we exclude Day 45 for the moment, each of the ULS-15 drafts show periods of nearly uniform returns. For Day 78, these occur throughout almost the entire hour; for Days 79 and 90, they occur during the half-hour interval following t_{SAR} . For these periods of uniform ice thickness, we calculate the average drafts and their standard deviations as listed in the table.

[50] For Day 45, because at t_{SAR} there is a large ice floe immediately adjacent to ULS-15, and because of the large range of ice drafts at ULS-15 within the 1-hour period, the choice of a representative ice draft is more difficult. There are at least two ways to choose this thickness. The first is to take the average of the minimum values in the sequence, which yields a frazil draft of 0.38 ± 0.05 m. The second is to take the mean of all drafts for which the first and last valid return differ by less than ± 0.01 m. This assumes that the ice satisfying this criterion is a frazil slurry that cannot maintain differences in thickness over the horizontal scale of the ULS field-of-view. This estimate yields a draft of 0.5 ± 0.2 m, which is listed in the table. Table 2 converts these drafts to h_C by multiplying the draft by 0.4, then dividing it by 0.92. The resultant range of the frazil accumulation thickness varies from 0.1 to about 0.2 m.

[51] The next-to-last column shows the observed polynya width, which is measured from SAR imagery in the vicinity of the ULSs at approximately ± 10 km to the east and west of their position. Finally, the last column gives the calculated polynya width from equation (1). In this column, the uncertainties are only from the ice drafts, where we ignore the unknown uncertainties associated with the ice drift and meteorology. Comparison of the last two columns shows that with the exception of Day 79, the observed and predicted polynya widths approximately agree. The lack of agreement for Day 79 may be due to the decrease in wind velocity between Days 78 and 79, so that the ice drift velocity is too large for the Day 79 calculation. With this exception, the table provides the first field validation of the Pease equation.

[52] The above calculation uses the fresh water latent heat of freezing, consistent with Pease [1987]. If instead we follow Haarpaintner et al. [2001] and assume that the young, accumulated ice has a 10% brine volume, then the solid ice equivalent values of h_C are reduced by 13% and the polynya width is reduced by the same percentage. This improves the agreement in the first two cases, maintains it for the fourth and suggests that future models of polynya processes need to consider such small-scale processes. Of equal importance, the table shows that h_C increases with wind speed, where $U = 8 \text{ m s}^{-1}$ yields 0.10 m and $15\text{--}20 \text{ m s}^{-1}$ yields 0.20 m. This increase is consistent with work by

Bauer and Martin [1983], the laboratory experiments of Martin and Kaufman [1981] and the model of Winsor and Björk [2000]. These observations strongly support the Pease relation, and also support the assumption that the frazil accumulation depth increases with wind speed.

7. Comparison of Near-Freezing and Supercooled Temperatures With Deep Scattering Events

[53] As Table 2 shows, SeaBird conductivity/temperature sensors were moored beneath each ULS, as well as at the near-coastal stations P1 and P2. Throughout their deployment, the SeaBirds produced hourly-averaged values of the water temperature T and salinity S . Both Table 2 and Figure 1 show that P2 is best situated to observe the temperature consequences of deep scatterers; of the four SeaBirds, it is closest to the coast and at about the same depth as the ULSs. Also, during periods of frazil formation, it is upwind of the ULSs and outside of the Kookooligit Mountain wind shadow described by Walter [1989]. Although P1 is at the same depth as P2, it is further from the coast and in the wind shadow. Because the other two SeaBirds are mounted below the ULSs at greater depths than P1 and P2, they may be relatively insensitive to the occurrence of frazil above them in the water column.

[54] For each of the SeaBirds, Figure 8 shows the time series of the difference between the observed and the freezing temperature, where the freezing temperature was calculated using a standard algorithm with the input of in situ depth, S and T [Millero, 1978; Gill, 1982, Appendix]. During the 90-day period, the observed salinities varied by about 2 psu. In editing these data, there were several short periods when the conductivity sensor head apparently became fouled; this was apparent because the instrument record showed a constant salinity followed by a step. These events were removed from the time series, and replaced by gaps. The bottom of the ULS-15 and ULS-42 SeaBird sub-figures is the line $\Delta T_F = 0.00^{\circ}\text{C}$; for the P1 and P2 sub-figures, the dashed line shows the $\Delta T_F = 0.00^{\circ}\text{C}$ line. Also on each subfigure, the dotted line shows $\Delta T_F = 0.01^{\circ}\text{C}$.

[55] As Figure 3 shows, FP1 and FP5 were the deepest scattering events observed by the ULSs. For these periods, examination of the ULS-15 and ULS-42 SeaBird time series show that the temperatures at both instruments fell to within 0.01°C of freezing during FP1, and at the ULS-15 SeaBird during FP5, so that the S , T and ULS ice draft observations are consistent with freezing water and the presence of frazil crystals at depth. For the nearshore SeaBirds, both P1 and P2 observed supercooling during FP1, with more supercooling at P2. For FP5, P2 observed supercooling, and P1

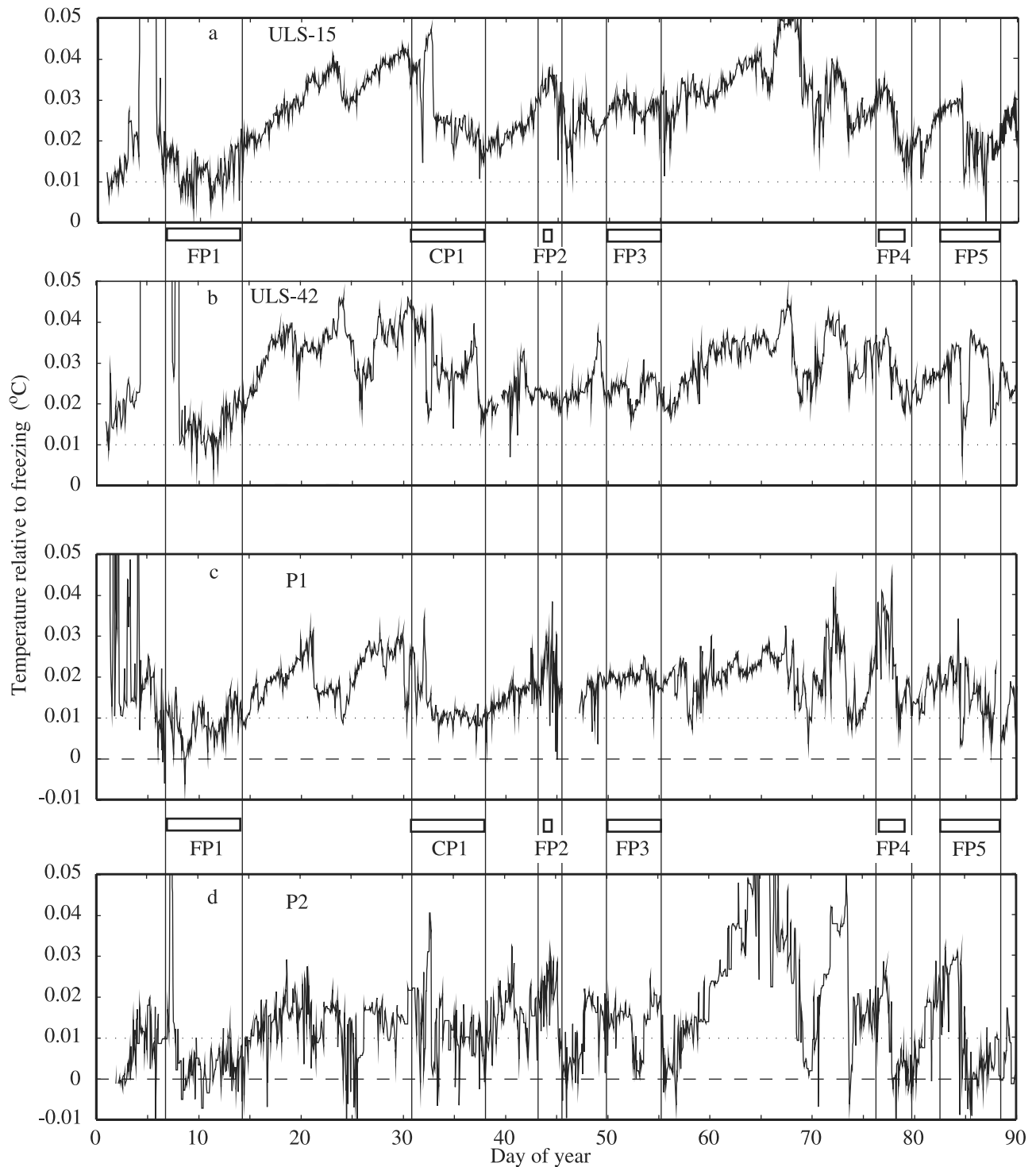


Figure 8. The water temperature relative to freezing determined at the SeaBird instrument depths for four locations, (a) ULS-15, (b) ULS-42, (c) P1, and (d) P2. On the figures, the horizontal dotted lines show a relative temperature of 10^{-2} K; on Figures 8a and 8b, the bottom of the figure is the freezing point; on Figures 8c and 8d, the dashed line is the freezing point. The vertical lines mark the polynya events, which are identified by the labels below Figures 8a and 8c. See text for additional description.

observed temperatures within 0.01°C of freezing. For the other events, P2 observed supercooling following FP3 and during FP4. Even though the temperatures at P1 and P2 are close to freezing, no supercooling occurs during CP1. The

greater occurrence of supercooling at P2 than at P1 is consistent with P1 being outside the wind shadow and closer to shore. Although these observations of supercooled and near-freezing water do not eliminate air bubbles as a

source of deep scatterers, they make the possibility of frazil ice at depth more likely.

8. Summary and Conclusions

[56] We compare AVHRR, SAR, ULS, and SeaBird salinity/temperature measurements from the St. Lawrence Island polynya during periods of frazil and congelation ice formation, and use the AVHRR to retrieve ice thicknesses. For smooth and lightly ridged congelation ice, the thermal and ULS ice thicknesses agree within the observational uncertainty. For periods when the SAR images show frazil crystals being herded into long plumes over the ULS positions, the ULSs observe scatterers at depths as great as 20 m and the SeaBirds observe water temperatures that are either supercooled or very close to freezing. Although we cannot eliminate air bubbles as a source of scattering, the suppression of breaking waves by surface frazil ice combined with observations of deep scatterers and supercooling at depth are consistent with frazil at depth. Whether this frazil forms at depth or is advected into the water column by the Langmuir circulation cannot be determined from the present observations.

[57] The combination of the ULS thickness measurements with the SAR and meteorological observations allows the determination of all of the variables used in the steady state polynya models; namely, the pack ice advection, the accumulation thickness, the frazil ice growth rate and the polynya width. From four polynya cases we find that the observed frazil ice accumulation thickness is between 0.1 and 0.2 m, and that in three of these cases, the calculated polynya widths approximately agree with the observed. The accumulation thickness also increases with wind speed. This is the first validation of the Pease relation, and also supports much of the numerical and analytical modeling of polynyas done since her paper. The use of this field technique in the future and especially in cooperation with numerical modeling efforts should yield improved models of polynyas and a greater understanding of their role in air/sea transfer.

Appendix A: Operation of the Upward Looking Sonars

[58] The ULS emits a vertically-propagating pulse of acoustic energy, then measures the time for the pulse to propagate to the target and back. A fixed gain is applied to the received signal, and a target is detected when the receiver voltage first exceeds a fixed threshold. The ULS listens for the reflected signal in a temporal window that corresponds to targets at depths between 20 m below sea level and 2.1 m above.

[59] For each pulse, the ULS measures six variables: the output of a precision pressure gauge, the sonar distance to the nearest target in the window, the sonar distance to the furthest distinct target in the window, the total count of distinct threshold crossings, the total count of valid threshold crossings and a match indicator. "Valid" variables are those for which the received signal voltage remains above the threshold at each of seven consecutive 100-ms intervals following the initial threshold crossing. The quantities recorded by the ULS are derived from pairs of pulses emitted in rapid succession. For each set of pulses, the ULS measures

the first and last valid return defined in section 2. The last valid return ice drafts obtained in a given pair of pulses are compared, and if they differ by less than 16 cm they are averaged, the match indicator is set to 1, the variables are recorded, and the ULS waits until the next measurement time. If a matched pair of last valid return ice drafts is not obtained from a pair of pulses, another pair is emitted and processed. After three unsuccessful tries, the match indicator is set to zero, the available variables are recorded, and the ULS waits until the next measurement time.

[60] If h_1 is the depth of the ULS below sea level estimated from the pressure gauge, and h_2 the distance or range between the ULS and the target as estimated from the sonar returns, then the ice draft h is

$$h = h_1 - h_2, \quad (\text{A1})$$

where h is determined for both the first and last valid returns.

A1. Processing of the ULS Data

[61] The first step in processing the data is to convert the quantities stored in the ULS onboard memory into units of time and pressure, using the calibration coefficients for the ULS clock and the precision pressure gauge. The measured pressure p_p is referred to sea level by subtraction of the sea level atmospheric pressure p_{slp} interpolated to the ULS position and time from the NCEP (National Center for Environmental Prediction) 1200 UT analyses,

$$p = p_p - p_{slp}. \quad (\text{A2})$$

The sonar elapsed times τ are converted to distances according to

$$h_2 = \bar{c}\tau/2, \quad (\text{A3})$$

where \bar{c} is the average sound speed in the water column above the ULS. For this analysis, \bar{c} is computed from the measured T , S and p_p , using the equation of state from Gill [1982, Appendix].

[62] The depth h_1 is then computed using the hydrostatic equation

$$h_1 = \rho/\bar{\rho}g - K, \quad (\text{A4})$$

where $\bar{\rho}$ is the average density of the water column above the ULS, also computed from the measured T and S , g is the acceleration of gravity and $K = 0.42$ m is the vertical distance between the sonar transducer and the pressure port on the ULS.

A2. Sources of ULS Error

[63] A rational discussion of measurement errors requires clear definitions for the quantities to be measured. Ice draft is defined as the vertical distance from bottom of the ice to sea level, at each point in time and horizontal space. The "bottom" of the ice is defined as the lowest ice in the column at that point. Ice thickness is defined as the vertical distance from the bottom of the ice to the top of the ice. These definitions do not refer to the density of the ice, or to the nature of the material that may intervene between the "bottom" and the "top". For frazil ice, much of this inter-

vening material is liquid seawater. In the case of deformed ice, the intervening material frequently includes liquid seawater, air and snow. Variations in the ice density and the volume of intervening material strongly affect the relationship between ice draft and other properties one might derive from it, such as ice volume, ice mass, thermal conductivity, and salt content. Typically, these relationships are strongest when the ice takes the form of a nearly uniform, horizontal slab of congelation ice. Therefore, to make best use of measurements with the ULS, AVHRR or any ice sensor, it is important to have information on the “type” of ice as well as its draft and thickness. For this reason, we divide the discussion of ULS errors into two categories: errors of target identification and the random instrument errors.

[64] The targets that we wish to detect with the ULS are of two kinds: water/ice interfaces and water/air interfaces. Errors occur when the ULS detects a target that does not fall into either category. These “false targets” may include air bubbles, zooplankton, fish, and sediment. Even when the target is ice, it is important to distinguish frazil ice, deformed ice and undeformed ice. One approach to distinguishing these types is to compare the first and last valid return ice drafts. Undeformed sea ice and flat open water are targets for which the first and last valid thicknesses should and do agree to within at most a few centimeters. By contrast, air bubbles, fish, zooplankton, sediment and frazil ice tend to produce multiple returns, either through volume scattering or because these targets are not uniformly distributed in the sonar beam. Therefore a large difference between last valid and first return draft puts a given data point in question. Unfortunately, such large differences can also occur when the target is deformed sea ice. Air bubbles and sediment occurrence tend to be associated with wind acting directly on the liquid surface, so these targets are assumed negligible during the winter period.

[65] The random measurement errors divide into environmental and instrument uncertainties. The environmental uncertainties are as follows. Typical RMS errors in the NCEP sea level pressure analysis are in the range 2–3 mbar, which translates to a thickness error of ± 2 –3 cm. The variations in T, S can be very significant, but in this study these parameters were measured continuously just below the ULS, and the water column is expected to remain well mixed during winter. Therefore these errors, though hard to quantify, are probably smaller than the error in surface level pressure. Errors in ice draft can also arise if the sonar beam is not vertically oriented, but because the transducer is mounted on a weighted gimbal inside the lens, these errors are negligible. The largest error associated with the absolute calibration, tolerance, and stability of the ULS components is the round-off error in the pressure gauge, which amounts to ± 2 cm. Summation of these two terms yields a total RMS error for a single observation of about ± 4 cm; when the thicknesses are averaged, the round-off error becomes negligible, while the contribution from the error associated with the sea level air surface pressure remains constant.

[66] **Acknowledgments.** We thank Esther Munoz for help with the meteorological data, and Kevin Engle and the Alaska Geophysical Institute for providing us with the SAR and AVHRR data, and Harry Stern for help with the SAR data. We thank Tom Weingartner for allowing us to use the SeaBird data from P1, Seth Danielson for help with the SeaBird and bottom topography data, and Knut Aagaard and Rebecca Woodgate for use of and

help with the SeaBird data from P1, ULS-15 and ULS-42, and Kay Runciman for processing the ULS data. We also thank our anonymous reviewer for helpful comments, and thank Joerg Haarpaintner for pushing us until we got it right. R. M. acknowledges the support of NSF under grant OPP-0084287; S. M. and R. D. acknowledge the support of the National Science Foundation under OCE9811097 and of NASA under grant NAG5-11067.

References

- Bauer, J., and S. Martin, A model of grease ice growth in small leads, *J. Geophys. Res.*, *88*, 2917–2925, 1983.
- Biggs, N. R. T., A. M. Morales Maqueda, and A. J. Willmott, Polynya flux model solutions incorporating a parameterization for the collection thickness of consolidated new ice, *J. Fluid Mech.*, *408*, 179–204, 2000.
- Crawford, G. B., and D. M. Farmer, On the spatial distribution of ocean bubbles, *J. Geophys. Res.*, *92*, 8231–8243, 1987.
- Farmer, D. M., and M. Li, Patterns of bubble clouds organized by Langmuir circulation, *J. Phys. Oceanogr.*, *25*, 1426–1440, 1995.
- Gill, A. E., *Atmosphere-Ocean Dynamics*, 662 pp., Academic, San Diego, Calif., 1982.
- Grenfell, T. C., and G. A. Maykut, The optical properties of ice and snow in the Arctic Basin, *J. Glaciol.*, *18*(80), 445–463, 1977.
- Haarpaintner, J., J.-C. Gascard, and P. M. Haugan, Ice production and brine formation in Storfjorden, Svalbard, *J. Geophys. Res.*, *106*, 14,001–14,013, 2001.
- Hudson, R. D., Annual measurement of sea-ice thickness using an upward-looking sonar, *Nature*, *344*, 135–137, 1990.
- Key, J., and M. Haefliger, Arctic ice surface temperature retrieval from AVHRR thermal channels, *J. Geophys. Res.*, *97*, 5885–5893, 1992.
- Key, J., J. Collins, C. Fowler, and R. Stone, High-latitude surface temperature estimates from thermal satellite data, *Remote Sens. Environ.*, *61*, 302–309, 1997.
- Liu, T. K., S. Martin, C. Y. Peng, and R. Kwok, Tracking of ice edges and ice floes by wavelet analysis of SAR images, *J. Atmos. Oceanic Technol.*, *14*, 1187–1198, 1997.
- Martin, S., Frazil ice in rivers and oceans, *Annu. Rev. Fluid Mech.*, *13*, 379–397, 1981.
- Martin, S., and P. Kaufman, A field and laboratory study of wave damping by grease ice, *J. Glaciol.*, *27*, 283–313, 1981.
- Martin, S., R. Drucker, and K. Yamashita, The production of ice and dense shelf water in the Okhotsk Sea polynyas, *J. Geophys. Res.*, *103*, 27,771–27,782, 1998.
- Melling, H., P. H. Johnston, and D. A. Riedel, Measurements of the underside topography of sea ice by moored subsea sonar, *J. Atmos. Oceanic Technol.*, *12*(3), 589–602, 1995.
- Millero, F. J., Freezing point of seawater, in *Eighth Report of the Joint Panel on Oceanographic Tables and Standards*, UNESCO Tech. Pap. Mar. Sci. 28 (Annex 6), Paris, 1978.
- Morales Maqueda, M. A., and A. J. Willmott, A two-dimensional model of a wind-driven coastal polynya: Application to the St. Lawrence Island polynya, *J. Phys. Oceanogr.*, *30*, 1281–1304, 2000.
- Overland, J. E., and R. L. Colony, Geostrophic drag coefficients for the central Arctic derived from Soviet drifting station data, *Tellus, Ser. A*, *46*, 75–85, 1994.
- Pease, C. H., The size of wind-driven coastal polynyas, *J. Geophys. Res.*, *92*, 7049–7059, 1987.
- Pilkington, G. R. and B. D. Wright, Beaufort Sea ice thickness measurements from an acoustic, under-ice, upward-looking ice keel profiler, paper presented at First International Offshore and Polar Engineering Conference, Int. Soc. of Polar and Offshore Eng., Edinburgh, 1991.
- Schumacher, J. D., K. Aagaard, C. H. Pease, and R. B. Tripp, Effects of a shelf polynya on flow and water properties in the northern Bering Sea, *J. Geophys. Res.*, *88*, 2723–2732, 1983.
- Strass, V. H., Measuring sea ice draft and coverage with moored upward looking sonars, *Deep Sea Res., Part I*, *45*, 795–818, 1998.
- Vinje, T., N. Nordlund, and A. Kvambekk, Monitoring ice thickness in Fram Strait, *J. Geophys. Res.*, *103*, 10,437–10,449, 1998.
- Walter, B. A., A study of the planetary boundary layer over the polynya downwind of St. Lawrence Island in the Bering Sea using aircraft data, *Boundary Layer Meteorol.*, *48*, 255–282, 1989.
- Winsor, P., and G. Björk, Polynya activity in the Arctic Ocean from 1958 to 1997, *J. Geophys. Res.*, *105*, 8789–8803, 2000.
- Yu, Y., and D. A. Rothrock, Thin ice thickness from satellite thermal imagery, *J. Geophys. Res.*, *101*, 25,753–25,766, 1996.

R. Drucker and S. Martin, School of Oceanography, University of Washington, Box 357940, Seattle, WA 98195-7940, USA. (seelye@ocean.washington.edu)

R. Moritz, Polar Science Center/Applied Physics Laboratory, University of Washington, Seattle, WA 98105-6698, USA.